SUPERCONDUCTIVITY

Discovery of orbital-selective Cooper pairing in FeSe

P. O. Sprau,[1,2]* A. Kostin,[1,2]* A. Kreisel,[3,4]* A. E. Böhmer,[5] V. Taufour,[5]† P. C. Canfield,[5,6] S. Mukherjee,[7]‡ P. J. Hirschfeld,[8] B. M. Andersen,[3] J. C. Séamus Davis[1,2,9,10]§

The superconductor iron selenide (FeSe) is of intense interest owing to its unusual nonmagnetic nematic state and potential for high-temperature superconductivity. But its Cooper pairing mechanism has not been determined. We used Bogoliubov quasiparticle interference imaging to determine the Fermi surface geometry of the electronic bands surrounding the $\Gamma = (0, 0)$ and $X = (\pi/a_{Fe}, 0)$ points of FeSe and to measure the corresponding superconducting energy gaps. We show that both gaps are extremely anisotropic but nodeless and that they exhibit gap maxima oriented orthogonally in momentum space. Moreover, by implementing a novel technique, we demonstrate that these gaps have opposite sign with respect to each other. This complex gap configuration reveals the existence of orbital-selective Cooper pairing that, in FeSe, is based preferentially on electrons from the d_{yz} orbitals of the iron atoms.

The high-temperature superconductivity in iron-based superconductors is typically most robust where coexisting antiferromagnetic and nematic ordered states are suppressed by doping or pressure (*1*–*3*). However, FeSe appears to be distinctive for several reasons: (i) Although strongly nematic, it does not form an ordered magnetic state and is instead hypothesized to be a quantum paramagnet (*4*–*6*); (ii) it exhibits evidence for orbital selectivity (*7*, *8*) of band structure characteristics (*9*–*12*); and (iii) a monolayer of FeSe grown on a $SrTiO_3$ substrate has the highest critical temperature T_c of all iron-based superconductors (*13*–*16*). It is therefore essential to understand the electronic structure and superconductivity of FeSe at a microscopic level; however, the Cooper pairing mechanism of FeSe has thus far been unknown. A quantitative determination of the momentum-space ($\vec{k}$-space) structure and relative sign of the superconducting energy gaps $\Delta_i(\vec{k})$ on each electronic band $E_i(\vec{k})$ is necessary to identify this mechanism. So far, this has not been achieved because of the minute Fermi surface pockets, as well as the highly anisotropic $\Delta_i(\vec{k})$ requiring an energy resolution $\delta E < 100$ μeV. In this work, we used subkelvin Bogoliubov quasiparticle interference (BQPI) imaging (*17*–*19*), an established technique for high-precision multiband $\Delta_i(\vec{k})$ determination (*20*–*22*), to measure the detailed structure of the energy gaps in FeSe.

In the orthorhombic phase below the structural transition temperature $T_S \cong 90$ K, FeSe has a crystal unit cell with conventional lattice parameters $a = 5.31$ Å, $b = 5.33$ Å, and $c = 5.48$ Å. We parameterize the Fe plane of the same lattice by using the two inequivalent Fe-Fe distances $a_{Fe} = 2.665$ Å and $b_{Fe} = 2.655$ Å in the orthorhombic, nematic phase [Fig. 1A and section I of (*23*)]; we define the x axis (y axis) to always be parallel to the orthorhombic a_{Fe} axis (b_{Fe} axis), so that our x-y coordinate system rotates when a twin boundary is crossed. The FeSe Fermi surface is postulated to consist of three bands—α, ε, and δ (shown for $k_z = 0$ in Fig. 1B)—and may be parameterized accurately using a tight-binding model (*24*, *25*) that is fit simultaneously to several types of experimental observations [sections II and III of (*23*)]. Surrounding the $\Gamma = (0, 0)$ point is an ellipsoidal hole-like α-band, whose Fermi surface $\vec{k}_\alpha(E = 0)$ has its major axis aligned to the orthorhombic b_{Fe} axis; surrounding the $X = (\pi/a_{Fe}, 0)$ point is the electron-like ε-band whose "bowtie" Fermi surface $\vec{k}_\varepsilon(E = 0)$ has its major axis aligned to the orthorhombic a_{Fe} axis. At the $Y = (0, \pi/b_{Fe})$ point, a δ-band Fermi surface should also exist if its quasiparticles are coherent, but it has not been detectable by spectroscopic techniques. In this picture, the d_{yz} orbital content of the α-band Fermi surface has its maximum value along the x axis (green in Fig. 1B), whereas its d_{xz} orbital content peaks along the y axis (red in Fig. 1B) (*25*). Conversely, the d_{yz} orbital content of the ε-band Fermi surface is maximum along the y axis (green in Fig. 1B), and its d_{xy} orbital content reaches its highest point along the x axis (blue in Fig. 1B) [(*24*–*26*) and section II of (*23*)]. These α-band and ε-band Fermi surface pockets (Fig. 1B) exhibit maximal simultaneous consistency with Fermi surface geometry from angle-resolved photoemission spectroscopy (ARPES) (*26*, *27*), quantum oscillations (*28*, *29*), and our BQPI imaging, as discussed below and in section III of (*23*).

A fundamental issue in iron-based superconductivity research is whether conduction electrons are weakly or strongly correlated and what the consequences thereof are for enhancing the superconductivity. The situation is complex because multiple Fe orbitals (e.g., d_{xz}, d_{yz}, and d_{xy}) are involved. One limit of theoretical consideration is an uncorrelated metallic state where "nesting" features of the Fermi surface geometry generate antiferromagnetic spin fluctuations, which then mediate Cooper pairing and superconductivity (*2*). In contrast, the ordered magnetic states of these same materials are often modeled using frustrated multi-orbital Heisenberg (J_1-J_2) models in which electrons are essentially localized, with the metallicity and spin fluctuation–mediated superconductivity appearing upon doping this magnetic insulator (*5*). Intermediate between the two is the Hund's metal viewpoint (*7*) in which strong Hund's coupling, while aligning the Fe spins, also suppresses the interorbital charge fluctuations. This generates orbital decoupling in the electronic structure, which allows "orbital selectivity" to occur in the effects of correlations (*7*, *8*). In theory, the result can be Mott-localized states associated with one orbital coexisting with delocalized quasiparticle states associated with others. Under such circumstances, the pairing itself can become orbital-selective (*30*, *31*), meaning that the electrons of predominantly one specific orbital character bind to form the Cooper pairs of the superconductor. If this occurs, the superconducting energy gaps should become highly anisotropic (*30*, *31*), being large only for those Fermi surface regions where a specific orbital character dominates. Such phenomena have remained largely unexplored because orbital-selective Cooper pairing has never been detected in any material.

To search for such pairing in FeSe, we applied BQPI imaging of impurity-scattered quasiparticles that interfere quantum-mechanically to produce characteristic modulations of the density of states, $N(\vec{r}, E)$ (where $\vec{r}$ is location), surrounding each impurity atom. When a $\vec{k}$-space energy gap $\Delta_i(\vec{k})$ is anisotropic, the Bogoliubov quasiparticle dispersion $E_i(\vec{k})$ will exhibit closed constant-energy contours (CECs), which are roughly banana-shaped and surround Fermi surface points where $\Delta_i(\vec{k})$ is minimum (*20*–*22*). Then, at a given energy E, the locus of the "banana tips" can be determined because the maximum-intensity BQPI modulations occur at wave vectors $\vec{q}_j(E)$ connecting the tips, thanks to their high joint density of states for scattering interference. The superconductor's Cooper-pairing energy gap $\Delta_i(\vec{k})$ and the Fermi surface on each band are then determined directly (*20*–*22*) by geometrically inverting the

---

[1]Laboratory of Atomic and Solid State Physics, Department of Physics, Cornell University, Ithaca, NY 14853, USA. [2]Condensed Matter Physics and Materials Science Department, Brookhaven National Laboratory, Upton, NY 11973, USA. [3]Niels Bohr Institute, University of Copenhagen, Juliane Maries Vej 30, DK 2100 Copenhagen, Denmark. [4]Institut für Theoretische Physik, Universität Leipzig, D-04103 Leipzig, Germany. [5]Ames Laboratory, U.S. Department of Energy, Ames, IA 50011, USA. [6]Department of Physics and Astronomy, Iowa State University, Ames, IA 50011, USA. [7]Department of Physics, Binghamton University–State University of New York, Binghamton, NY, USA. [8]Department of Physics, University of Florida, Gainesville, FL 32611, USA. [9]School of Physics and Astronomy, University of St Andrews, Fife KY16 9SS, Scotland. [10]Tyndall National Institute, University College Cork, Cork T12R5C, Ireland.
*These authors contributed equally to this work. †Present address: Department of Physics, University of California–Davis, Davis, CA 95616, USA. ‡Department of Physics, Indian Institute of Technology Madras, Chennai 600036, India. §**Corresponding author. Email: jcseamusdavis@gmail.com**

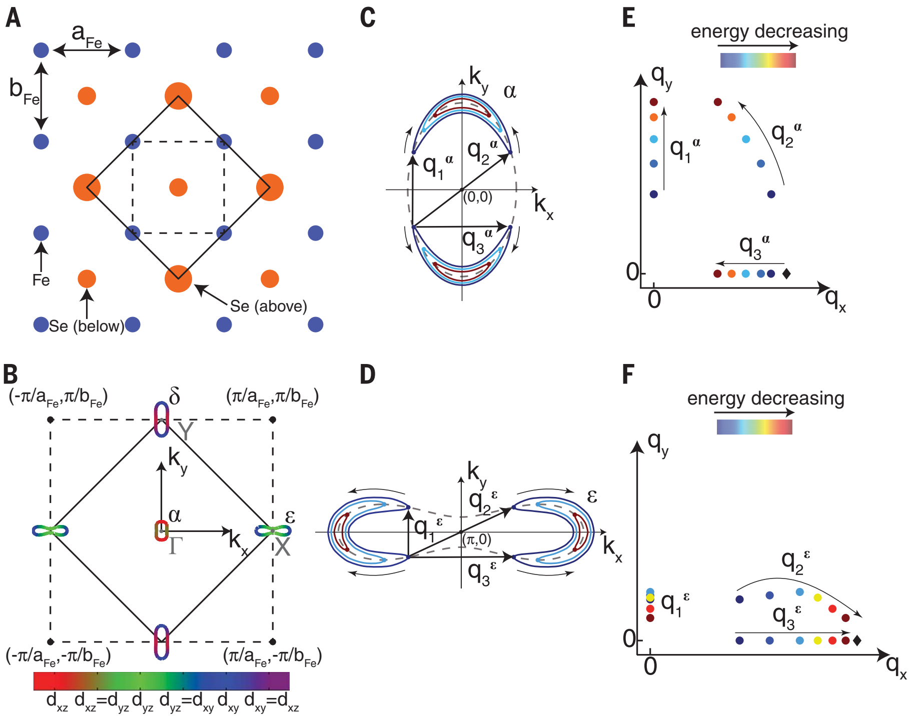

Fig. 1. Bogoliubov quasiparticle interference (BQPI) model for FeSe. (**A**) Top view of FeSe crystal structure. Dashed lines represent the 1-Fe unit cell, and solid lines show the actual unit cell. The unit cell of FeSe is distorted in the nematic phase with $a_{Fe} > b_{Fe}$. Throughout, we define the x axis, $\vec{k}_x$ axis, and $\vec{q}_x$ axis to all be parallel to the a_{Fe} axis, so that labels of orbitals such as d_{xy} or d_{yz}, or $\vec{k}$-space locations and states, are equally valid in both orthorhombic, nematic domains. (**B**) In the nematic phase with orthorhombic crystal symmetry, the FeSe Fermi surface consists of a hole-like α-band around Γ = (0, 0) and an electron-like ε-band around $X = (\pi/a_{Fe}, 0)$; the color code indicates the regions of Fermi surface dominated by states with primarily d_{yz} (green), d_{xz} (red), and d_{xy} (blue) orbital character. An anticipated third band, the δ-band around $Y = (0, \pi/b_{Fe})$, has not been observed by spectroscopic techniques. (**C**) Constant-energy contours (CECs) of Bogoliubov quasiparticles for the gapped α-band around Γ = (0, 0). The CECs are color-coded to indicate increasing energy (red to purple). A schematic ellipsoidal normal-state Fermi surface is shown using a gray dashed contour. Predominant scattering interference occurring between the "tips" of the banana-shaped CECs should produce a triplet of characteristic BQPI wave vectors: $\vec{q}_1^{\,\alpha}(E), \vec{q}_2^{\,\alpha}(E)$, and $\vec{q}_3^{\,\alpha}(E)$ (black arrows). (**D**) Same as (C), but for the gapped ε-band around $X = (\pi/a_{Fe}, 0)$. (**E**) The expected energy dependence of the α-band wave vector triplet $[\vec{q}_1^{\,\alpha}(E), \vec{q}_2^{\,\alpha}(E)$, and $\vec{q}_3^{\,\alpha}(E)]$ in (C); points are color-coded to indicate decreasing energy. The black diamond symbolizes the starting point of $\vec{q}_3^{\,\alpha}$, where Δ_α = max. (**F**) The expected energy dependence of the ε-band wave vector triplet $[\vec{q}_1^{\,\varepsilon}(E), \vec{q}_2^{\,\varepsilon}(E)$, and $\vec{q}_3^{\,\varepsilon}(E)]$ color-coded by energy. The black diamond symbolizes the end point of $\vec{q}_2^{\,\varepsilon}$, where Δ_ε = min.

measured BQPI wave vector set $\vec{q}_j(E)$ in the energy range $\Delta_i^{\min} < E < \Delta_i^{\max}$. Because these techniques can be implemented at temperatures $T \leq$ 300 mK, the $\Delta_i(\vec{k})$ on multiple bands can be measured with an energy resolution $\delta E \approx 75\ \mu\text{eV}$ (*21*, *22*), a precision unachievable by any other approach.

However, no BQPI measurements have been reported for bulk FeSe, although photoemission data for the equivalent of the α-band do exist for a related compound, Fe(Se,S) (*32*). For guidance, we first consider a pedagogical model, while recalling that Fermi surfaces and energy-gap structures derived using BQPI imaging do not depend on any particular model (*20*–*22*). Given the α-band Fermi surface (dashed gray contour in Fig. 1C), supporting an anisotropic $\Delta_\alpha(\vec{k})$ that has C_2 symmetry (*32*, *33*), the CECs would be as shown by the colored curves in Fig. 1C, with quasiparticle energy increasing as indicated by the color code. The tips of each Bogoliubov CEC "banana" are indicated by colored dots, similarly representing increasing energy. Thus, we expect that a triplet of inequivalent BQPI wave vectors $\vec{q}_i^{\,\alpha}(E)$ (i = 1 to 3) should exist (black arrows in Fig. 1C). The anticipated energy dependence of $\vec{q}_i^{\,\alpha}(E)$ is shown schematically in Fig. 1E. For each energy $\Delta_i^{\min} < E < \Delta_i^{\max}$, the positions of the four CEC banana tips $[\pm k_x(E), \pm k_y(E)]_\alpha$ can be determined by inverting

$$\vec{q}_1^{\,\alpha} = (0, 2k_y) \tag{1}$$

$$\vec{q}_3^{\,\alpha} = (2k_x, 0) \tag{2}$$

$$\vec{q}_2^{\,\alpha} = (2k_x, 2k_y) \tag{3}$$

If a C_2-symmetric energy gap $\Delta_\delta(\vec{k})$ existed on a coherent δ-band surrounding $Y = (0, \pi/b_{Fe})$, it might be expected to behave comparably. A similar analysis (Fig. 1, D and F) applies to the "bowtie" ε-band Fermi surface surrounding $X = (\pi/a_{Fe}, 0)$ (dashed gray contour in Fig. 1D), with the anticipated energy dependence of $\vec{q}_i^{\,\varepsilon}(E)$ shown schematically in Fig. 1F.

To measure the Fermi surface and the superconducting gap structure and sign, we imaged differential tunneling conductance $dI/dV(\vec{r}, eV) \equiv g(\vec{r}, E)$ at T = 280 mK (where I is current, V is voltage, and e is the electron charge) both as a function of location $\vec{r}$ and electron energy E. Because the Fermi surface pockets are so small in area (Fig. 1B), the expected range of dispersive intraband BQPI wave vectors is very limited—$0 < |\vec{q}_i^{\,\alpha,\varepsilon}(E)| < 0.25(2\pi/a_{Fe})$—whereas the interband BQPI necessitates resolving wave vectors $\geq \pi/a_{Fe}$. To achieve the $\vec{q}$-space resolution $|\delta q_i^{\alpha,\varepsilon}| \leq 0.01(2\pi/a_{Fe})$ required to discriminate the energy evolution of BQPI on both the α-band and ε-band necessitates high-precision $g(\vec{r}, E)$ imaging in very large fields of view. We typically used fields between 60 by 60 and 90 by 90 nm [section IV of (*23*)]. Local maxima of $|g(\vec{q}, E)|$, the amplitude Fourier transform of $g(\vec{r}, E)$, were then used to determine the characteristic wave vectors $\vec{q}_i^{\,\alpha}(E)$ and $\vec{q}_i^{\,\varepsilon}(E)$ of dispersive modulations of BQPI. Figure 2A shows a typical example of measured $g(\vec{r}, E)$ with its $|g(\vec{q}, E)|$ in Fig. 2C. In this case, by using a low-resolution scanning tunneling microscope (STM) tip, we predominantly detected the BQPI signal corresponding to the α-band surrounding Γ = (0, 0) [a complete data set is shown in movie S1 and section IV of (*23*)]. The evolution of the BQPI triplet $\vec{q}_i^{\,\alpha}(E)$ (black crosses in Fig. 2C) in the range 2.3 meV > |E| > 0.8 meV at 280 mK is plotted in Fig. 2E. Analogous images for the ε-band, obtained using tips with very high spatial resolution that are sensitive to states at high $\vec{k}$, are shown in Fig. 2, B, D, and F [a complete data set is shown in movie S2 and section IV of (*23*)]. Because both $\vec{q}_2^{\,\alpha}(E)$ and $\vec{q}_2^{\,\varepsilon}(E)$ evolve to finite wave vectors $2\vec{k}_F^{\,\alpha}$ and $2\vec{k}_F^{\,\varepsilon}$, respectively, as $E \to 0$ (Fig. 2, E and F), FeSe superconductivity is demonstrably in the Bardeen-Cooper-Schrieffer limit, and not near the Bose-Einstein condensation limit where BQPI wave vectors must evolve to 0 as $E \to 0$. From the conventional $N(E) \equiv dI/dV(E)$ density-of-states spectrum at T = 280 mK (Fig. 2, G and H), we find that the maximum gap on any band is $\Delta_\alpha^{\max} = 2.3$ meV, whereas another coherence peak occurs at the gap maximum of a second band at $\Delta_\varepsilon^{\max} = 1.5$ meV. The maximum gaps were assigned to each band on the basis of the energy evolution of BQPI to the energy limit $E \to 2.3$ meV for the α-band and $E \to 1.5$ meV for the ε-band. Lastly, because no conductance was detected in the energy region $E \lesssim 150\ \mu\text{eV}$, $\Delta^{\min} \gtrsim 150\ \mu\text{eV}$ for all bands.

The Fermi surfaces for the α- and ε-bands were next determined using the fact that the $\vec{k}$-space loci of CEC banana tips from both $\Delta_\alpha(\vec{k})$

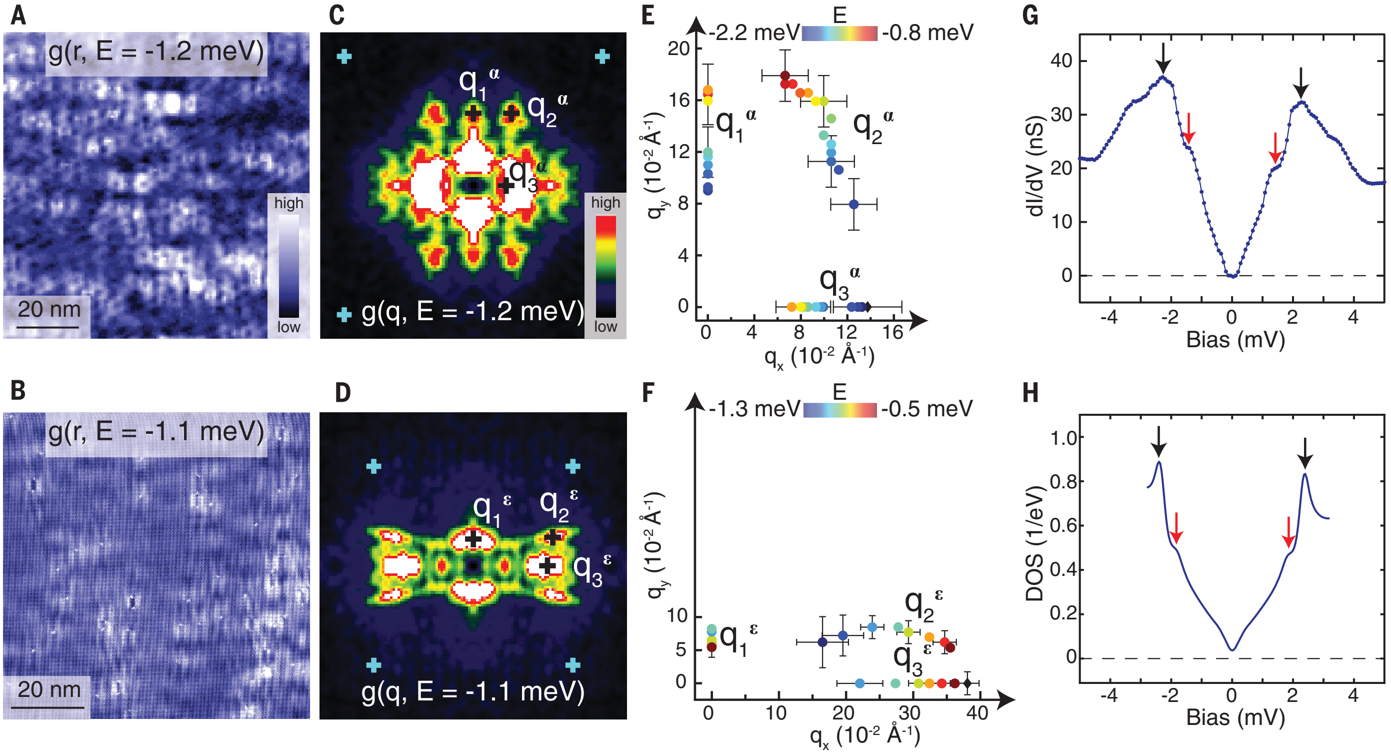

Fig. 2. Visualizing BQPI in FeSe. To achieve sufficient $\vec{q}$-space resolution, we use a field of view that is about 90 by 90 nm in which we image $g(\vec{r},E) \equiv dI/dV(\vec{r},E = eV)$ with bias modulation of 100 μV at T = 280 mK [section IV of (*23*)]. (**A**) Typical $g(\vec{r},E)$ measured using a low-resolution STM tip that is predominantly sensitive to α-band effects. (**B**) Typical $g(\vec{r},E)$ measured with tips with very high spatial resolution, which emphasize very-short-wavelength BQPI and are predominantly sensitive to ε-band effects. (**C**) Measured $|g(\vec{q},E)|$ derived from (A). The BQPI wave vector triplet $\vec{q}_i^{\,\alpha}(E)$ is identified by black crosses at the points of maximum amplitude. The blue crosses indicate the ($\pm 2\pi/8a_{Fe}$, $\pm 2\pi/8b_{Fe}$) points. (**D**) Measured $|g(\vec{q},E)|$ derived from (B). The BQPI triplet $\vec{q}_i^{\,\varepsilon}(E)$ is identified by black crosses at the points of maximum amplitude. The blue crosses indicate the ($\pm 2\pi/8a_{Fe}$, $\pm 2\pi/8b_{Fe}$) points. (**E**) Measured evolution of $\vec{q}_1^{\,\alpha}(E)$, $\vec{q}_2^{\,\alpha}(E)$, and $\vec{q}_3^{\,\alpha}(E)$. The $|g(\vec{q},E)|$ data are shown in movie S1. The black diamond is the first $\vec{q}_3^{\,\alpha}(E = -2.3\text{ meV})$ data point. (**F**) Measured evolution of $\vec{q}_1^{\,\varepsilon}(E)$, $\vec{q}_2^{\,\varepsilon}(E)$, and $\vec{q}_3^{\,\varepsilon}(E)$. The $|g(\vec{q},E)|$ data are shown in movie S2. The black diamond corresponds to the last $\vec{q}_2^{\,\varepsilon}(E = -0.3\text{ meV})$ data point. Representative error bars in (E) and (F) show the uncertainty of extracted wave vectors. (**G**) Measured $N(E) = dI/dV(E)$ density of states (DOS) spectrum. Black arrows indicate the maximum energy gap on any band, which we determine from BQPI to be on the α-band (Fig. 3). Red arrows indicate a smaller energy gap on a second band, which, from BQPI, is assigned to the ε-band (Fig. 3). (**H**) Calculated density of states $N(E)$ from the band structure and gap structure model used herein [sections II and VIII of (*23*)].

and $\Delta_\varepsilon(\vec{k})$ follow the Fermi surface of each band (Fig. 1) (*20–22*). The measured evolution of the BQPI wave vector triplets $\vec{q}_i^{\,\alpha}(E)$ and $\vec{q}_i^{\,\varepsilon}(E)$ is plotted in Fig. 2, E and F. The two Fermi surfaces of the α- and ε-bands of FeSe determined from BQPI imaging [section V of (*23*)] are shown in Fig. 3, A and B, using blue dots with errors bars for each measured point and blue curves for the Fermi surface. The area of the Fermi surfaces extracted by BQPI imaging is consistent with that at $k_z = 0$ [section III of (*23*) and fig. S5]. We schematically plot the measured magnitude of the energy gap $|\Delta_\alpha(\vec{k})|$ on the α-band in Fig. 3A and the measured magnitude $|\Delta_\varepsilon(\vec{k})|$ on the ε-band in Fig. 3B; in both cases, we use the width of the gray shaded region to indicate $|\Delta(\vec{k})|$ and include values of extrema of any energy gap from $N(E)$. Although exhibiting extraordinarily anisotropic ($\Delta_\alpha^{max}/\Delta_\alpha^{min} \gtrsim 15$) C_2-symmetric energy-gap structures, FeSe remains a fully gapped or nodeless (*34–38*) superconductor with gap minima $\Delta_{\alpha,\varepsilon}^{min} \gtrsim$ 150 μeV.

One of the key characteristics of iron-based superconductors is whether the energy gaps on different bands have opposite signs (*2*, *3*). For FeSe, this situation should be designated ± because the more conventional designation $s_\pm$ (*2*, *3*) is rendered inappropriate by the orthorhombic crystal symmetry. One technique for measuring ± pairing symmetry is to detect the enhancement in the amplitude of $g(\vec{q},E)$ at specific BQPI wave vectors when a magnetic field is applied; this was proposed to occur because field-induced scattering results in amplified quasiparticle interference between regions of $\vec{k}$-space with same-sign energy gaps (*39*). In Fe(Se,Te), this approach has yielded field-induced QPI intensity reduction for wave vectors linking the electron and hole pockets, indicative of ± pairing symmetry (*40*). Yet there are reservations about this interpretation (*41*) because (i) the wave vectors where the Fe(Se,Te) field-induced alternations are reported occur at Bragg points of the reciprocal lattice, and (ii) a microscopic explanation for these field-induced reductions is absent. To address these issues, another BQPI technique designed to determine ± pairing symmetry has been proposed (*41*). It is based on conventional (nonmagnetic) impurity scattering and the realization that the particle-hole symmetry of interband scattering interference patterns depends on the relative sign of the energy gaps on those bands (*41*). As a result, the energy-symmetrized $\rho_+(\vec{q},E)$ and energy-antisymmetrized $\rho_-(\vec{q},E)$ phase-resolved Bogoliubov scattering interference amplitudes

$$\rho_\pm(\vec{q},E) = \mathrm{Re}\left[g(\vec{q},+E)\right] \pm \mathrm{Re}\left[g(\vec{q},-E)\right] \quad (4)$$

have, at the $\vec{q}$ for interband scattering, distinct properties depending on the relative sign of the two gaps. Importantly, this approach, although not requiring variable temperature measurements, requires phase-resolved imaging of BQPI in order to reliably discriminate $\mathrm{Re}[g(\vec{q},E)]$ from $\mathrm{Im}[g(\vec{q},E)]$ (where Re is the real component and Im is the imaginary component). Moreover, the (anti)symmetrized functions $\rho_\pm(\vec{q},E)$ must be integrated over a particular $\vec{q}$-space region. Specifically, we focus on

$$\rho_-(E) = \sum_{\delta\vec{q}} \rho_-(\vec{p}_1 + \delta\vec{q},E) \quad (5)$$

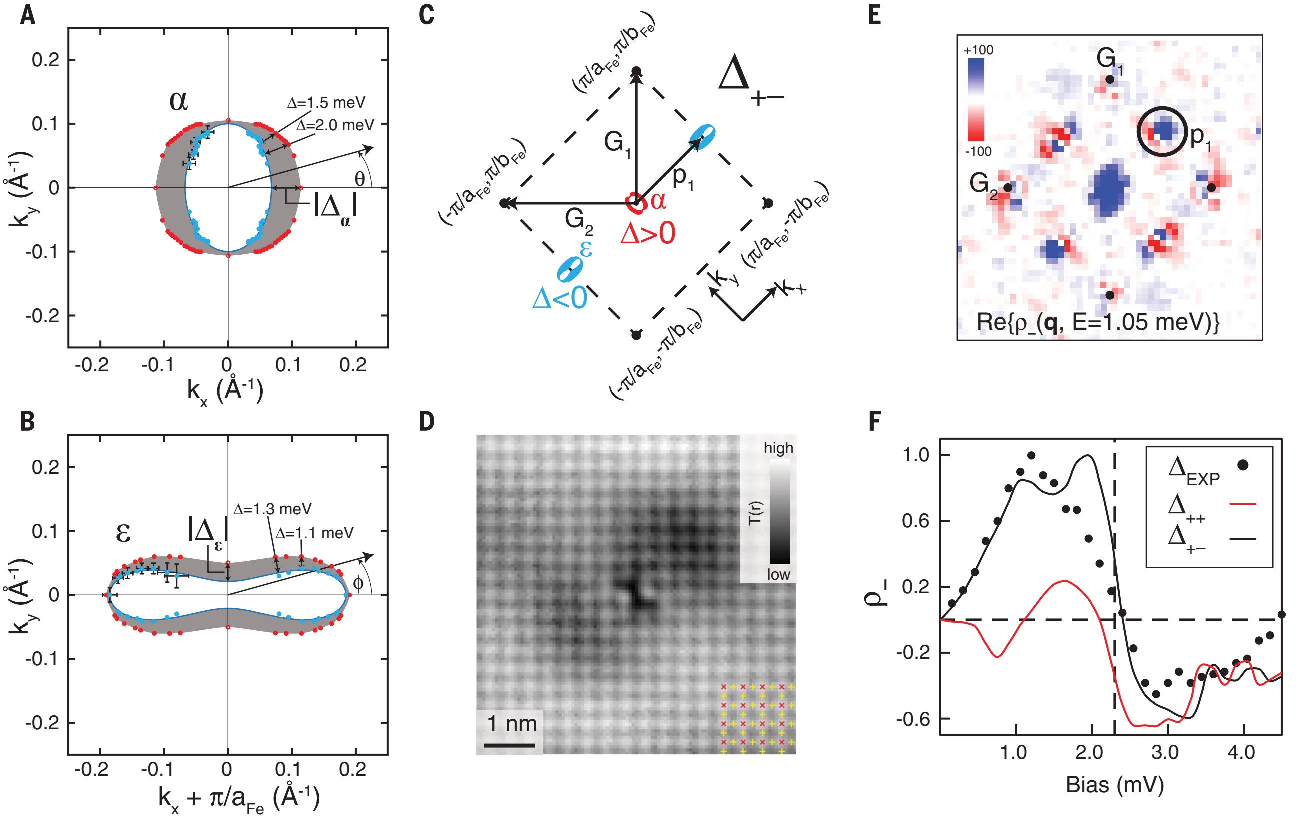

Fig. 3. BQPI determination of Fermi surfaces and energy gaps. The BQPI data analysis steps yielding the results shown here are explained in detail in section V of (*23*). (**A**) The Fermi surface of the α-band is measured using the BQPI triplet $\vec{q}_1^{\,\alpha}(E)$, $\vec{q}_2^{\,\alpha}(E)$, and $\vec{q}_3^{\,\alpha}(E)$ and shown as blue dots with representative error bars showing the uncertainty for each wave vector (red dots indicate superconducting gap magnitudes). The energy-gap magnitude for the α-band is measured using the energy dependence of the BQPI triplet $\vec{q}_1^{\,\alpha}(E)$, $\vec{q}_2^{\,\alpha}(E)$, and $\vec{q}_3^{\,\alpha}(E)$, plus the values of the maximum and minimum energy gap from $N(E)$ in Fig. 2G. (**B**) Same as (A), but for the ε-band using $\vec{q}_1^{\,\varepsilon}(E)$, $\vec{q}_2^{\,\varepsilon}(E)$, and $\vec{q}_3^{\,\varepsilon}(E)$. (**C**) $\vec{k}$-space schematics of FeSe interband scattering wave vector $\vec{p}_1$ between the α- and ε-bands, which connects gaps of opposite sign in the Δ_{+-} scenario. (**D**) Measured $T(\vec{r})$ topograph centered on a typical individual impurity site in a field of view ~6.5 by 6.5 nm. Red x's, surface (upper) Se sites; yellow pluses, Fe sites. (**E**) Typical measured $\rho_-(\vec{q},E) = \mathrm{Re}[g(\vec{q},+E)] \pm \mathrm{Re}[g(\vec{q},-E)]$ from BQPI $g(\vec{r},E)$ at E = 1.05 meV in the energy range within both Δ_α and Δ_ε. Complete $\rho_-(\vec{q},E)$ data are shown in movie S3. $\mathbf{G}_1$ and $\mathbf{G}_2$ are the reciprocal lattice vectors identified in (C). (**F**) The predicted $\rho_-(E)$ for ± pairing symmetry using the band-gap structure of FeSe [(A) and (B), and sections II, VI, and VIII of (*23*)] is shown as a solid black curve. The measured $\rho_-(E)$ for FeSe (black dots) is calculated by integration over the $\vec{q}$-space region identified by the black circle in Fig. 4E. The predicted $\rho_-(E)$ for no gap sign change in FeSe is shown as a solid red curve. The vertical dashed black line marks the energy of the maximum superconducting gap.

with radius δq confining $\vec{q}$-space to interband scattering processes between two distinct energy gaps (Fig. 3C). Given our quantitative knowledge of the Fermi surface and energy gaps of FeSe (Fig. 3, A and B), the $\rho_-(\vec{q},E)$ can be predicted specifically for this material, with the result shown as a solid black curve in Fig. 3F for the FeSe gaps $\Delta_\alpha(\vec{k})$ and $\Delta_\varepsilon(\vec{k})$ with ± pairing symmetry [section VI of (*23*)].

Experimentally, the challenge is then to achieve phase-resolved imaging of BQPI surrounding a single impurity atom in FeSe, such as an Fe site vacancy (*42*, *43*). Therefore, we measured $g(\vec{r},E)$ around individual impurity sites, each in a field of view ~6.5 by 6.5 nm (for example, Fig. 3D), and then mapped the $g(\vec{q},E)$ data onto a perfectly periodic atomic lattice. The $\vec{r}$-space origin of this lattice was then set at the impurity site (Fig. 3D) and $\rho_-(\vec{q},E) = \mathrm{Re}[g(\vec{q},+E)] - \mathrm{Re}[g(\vec{q},-E)]$ was measured. Figure 3E is a typical example of $\rho_-(\vec{q},E)$ [section VII of (*23*)]. Lastly, the $\rho_-(E)$ was determined from Eq. 5, with the integration radius δq chosen to capture only intensity related to scattering between $\Delta_\alpha(\vec{k})$ and $\Delta_\varepsilon(\vec{k})$ inside the black circle in Fig. 3E. The resulting $\rho_-(E)$ is shown as black dots in Fig. 3F. Comparison of this measured $\rho_-(E)$ with its predicted form for the FeSe gaps $\Delta_\alpha(\vec{k})$ and $\Delta_\varepsilon(\vec{k})$ with ± symmetry (solid black curve) shows them to be in good agreement, especially in that $\rho_-(E)$ for ± pairing symmetry does not cross zero within the range of energy gaps. Thus, within the framework of (*41*), these data demonstrate that the sign of $\Delta_\alpha(\vec{k})$ is opposite to that of $\Delta_\varepsilon(\vec{k})$.

The key results of our study are summarized in Fig. 4, A and B: The measured values of $\Delta_\alpha(\vec{k})$ and $\Delta_\varepsilon(\vec{k})$ are both extremely anisotropic but nodeless, each having C_2 symmetry with deep minima that are aligned along orthogonal crystal axes. Recalling that our x axis is defined to always be the orthorhombic a_{Fe} axis, we have found these results to be equally true in both nematic domains. Such a gap structure is highly divergent from conventional spin fluctuation pairing theory (*24*), which yields a weak, almost isotropic gap on the α-band and a strong gap on the ε-band but with an anisotropy of opposite $\vec{k}$-space orientation to that of the experimental data [section VIII of (*23*)].

However, orbital-selective pairing concentrated in the d_{yz} channel can provide an explanation for the observed $\Delta_\alpha(\vec{k})$ and $\Delta_\varepsilon(\vec{k})$. Figure 4B shows our measured angular dependence of $\Delta_\alpha(\vec{k})$ about Γ = (0, 0) and the equivalent for $\Delta_\varepsilon(\vec{k})$ about $X = (\pi/a_{\mathrm{Fe}}, 0)$. For a d_{yz} orbital-selective pairing interaction that peaks at wave vector $\vec{q} = (\pi/a_{\mathrm{Fe}}, 0)$, the predicted angular dependence of $\Delta_\alpha(\vec{k})$ and $\Delta_\varepsilon(\vec{k})$ is shown in Fig. 4C [section VIII of (*23*)], and its comparison with the measured $\Delta_\alpha(\vec{k})$ and $\Delta_\varepsilon(\vec{k})$ in Fig. 4B indicates the existence of orbital-selective Cooper pairing in FeSe.

Microscopically, such orbital-selective Cooper pairing may arise from differences in correlation strength for electrons with different orbital character. For example, correlations sufficient to generate incoherence for states with predominantly d_{xy} orbital character (*11*, *12*) would suppress their pairing within an itinerant picture. Moreover, superconducting FeSe must exhibit distinct quasiparticle

Fig. 4. Orbital-selective Cooper pairing in FeSe. (**A**) Measured k-space structure of anisotropic energy gaps of FeSe (Fig. 3). The red and blue colors indicate the different signs of the two gap functions. (**B**) Measured angular dependence of FeSe superconducting energy gaps $\Delta_\alpha(\vec{k})$ about $\Gamma = (0,0)$ and $\Delta_\varepsilon(\vec{k})$ about $X = (\pi/a_{Fe},0)$ from Fig. 3, A and B. Error bars show the energy uncertainty of extracted superconducting gap values. (**C**) Predicted angular dependence of $\Delta_\alpha(\vec{k})$ and $\Delta_\varepsilon(\vec{k})$ for an interband pairing interaction that peaks at $\vec{q} = (\pi/a_{Fe}, 0)$ and for which pairing is orbital-selective, occurring predominantly for electrons with d_{yz} orbital character [section VIII of (*23*)]. The dashed gray curves show the d_{yz} orbital character of states at the α-band and ε-band Fermi surfaces. These energy gap predictions are robust against variations in the quasiparticle orbital weights used in the theoretical calculations [section VIII of (*23*)], provided that the d_{yz} orbital is kept considerably more coherent than the d_{xz} orbital.

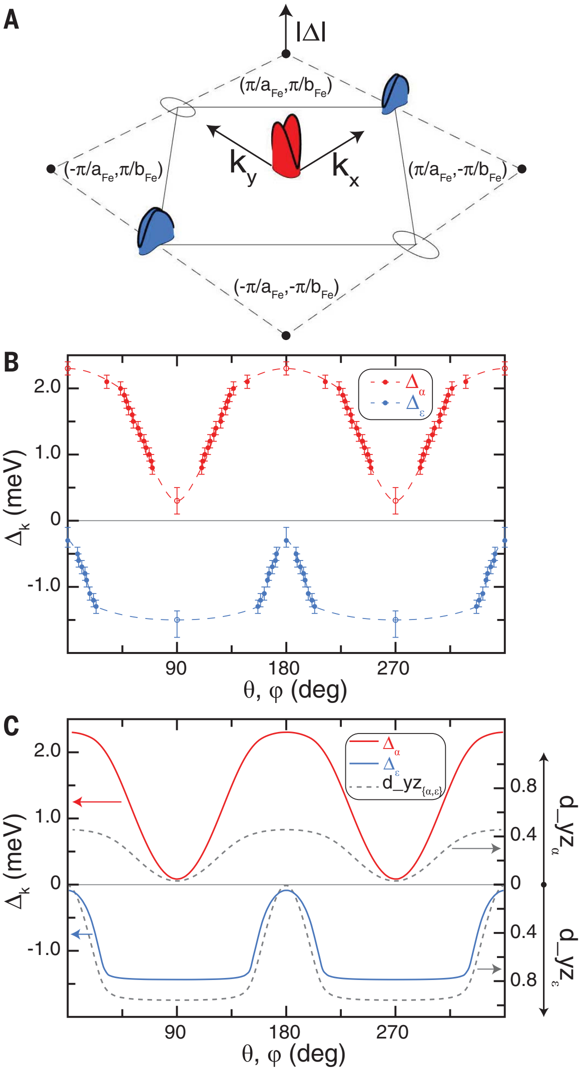

weights at the Fermi surface for states with d_{xz} and d_{yz} orbital character because of the nematic state (*15*, *16*). Under such circumstances, a Cooper pairing interaction focused at wave vector $\vec{q} = (\pi/a_{Fe}, 0)$, and forming spin-singlets from electrons predominantly with d_{yz} orbital character, can be modeled by enhancing the strength of the spin-fluctuation pairing interaction for electrons with d_{yz} orbital character relative to that for those with d_{xz} orbital character, while fully suppressing it for those with d_{xy} orbital character [(*24*) and section VIII of (*23*) for details]. In this case, the orbital selectivity of pairing arises from quasiparticle weights in the various channels of itinerant spin-fluctuation pairing theory, which are hypothesized to be very different owing to orbital-selective correlations [section VIII of (*23*)]. Such a model could explain why the δ-band, predominantly associated with the d_{xy} orbital, has weak visibility in ARPES (*11*, *12*) and BQPI (Figs. 2 and 3) observations and could also account for a low-energy spin susceptibility that is dominant at $\vec{q} = (\pi/a_{Fe}, 0)$, consistent with inelastic neutron scattering data (*44*). By projecting this form of orbital-selective pairing interaction onto the Fermi surfaces of FeSe (Fig. 3), the gap functions can be predicted by solving the linearized gap equation [(*24*) and section VIII of (*23*)]. The resulting predicted $\Delta_\alpha(\vec{k})$ and $\Delta_\varepsilon(\vec{k})$ (solid curves in Fig. 4C) are quantitatively consistent with the extremely anisotropic structure and sign reversal of the measured gap functions (Fig. 4, A and B). Moreover, because the magnitudes of $\Delta_\alpha(\vec{k})$ and $\Delta_\varepsilon(\vec{k})$ (solid curves in Figs. 4B) track the strength of d_{yz} orbital character on both bands (dashed curves in Fig. 4C) [(*24*–*26*) and section II of (*23*)], the influence of orbital selectivity on the Cooper pairing is directly manifest. Overall, these data reveal a distinctive and previously unknown form of correlated superconductivity based on orbital-selective Cooper pairing of electrons that, for FeSe, are predominantly from the d_{yz} orbitals of Fe atoms. Such orbital selectivity may be pivotal to understanding the microscopic interplay of quantum paramagnetism, nematicity, and high-temperature superconductivity in iron-based superconductors.

REFERENCES AND NOTES

1. J. Paglione, R. L. Greene, *Nat. Phys.* **6**, 645–658 (2010).
2. P. J. Hirschfeld, M. M. Korshunov, I. I. Mazin, *Rep. Prog. Phys.* **74**, 124508 (2011).
3. F. Wang, D.-H. Lee, *Science* **332**, 200–204 (2011).
4. F. Wang, S. A. Kivelson, D.-H. Lee, *Nat. Phys.* **11**, 959–963 (2015).
5. J. K. Glasbrenner *et al.*, *Nat. Phys.* **11**, 953–958 (2015).
6. Q. Wang *et al.*, *Nat. Commun.* **7**, 12182 (2016).
7. Z. P. Yin, K. Haule, G. Kotliar, *Nat. Mater.* **10**, 932–935 (2011).
8. L. de' Medici, G. Giovannetti, M. Capone, *Phys. Rev. Lett.* **112**, 177001 (2014).
9. M. Aichhorn, S. Biermann, T. Miyake, A. Georges, M. Imada, *Phys. Rev. B* **82**, 064504 (2010).
10. Z. K. Liu *et al.*, *Phys. Rev. B* **92**, 235138 (2015).
11. M. Yi *et al.*, *Nat. Commun.* **6**, 7777 (2015).
12. Z. Wang, V. Tsurkan, M. Schmidt, A. Loidl, J. Deisenhofer, *Phys. Rev. B* **93**, 104522 (2016).
13. Q.-Y. Wang *et al.*, *Chin. Phys. Lett.* **29**, 037402 (2012).
14. Z. Zhang *et al.*, *Sci. Bull.* **60**, 1301–1304 (2015).
15. D.-H. Lee, *Chin. Phys. B* **24**, 117405 (2015).
16. P. J. Hirschfeld, *C. R. Phys.* **17**, 197–231 (2016).
17. Q.-H. Wang, D.-H. Lee, *Phys. Rev. B* **67**, 020511(R) (2003).
18. Y. Y. Zhang *et al.*, *Phys. Rev. B* **80**, 094528 (2009).
19. A. Akbari, J. Knolle, I. Eremin, R. Moessner, *Phys. Rev. B* **82**, 224506 (2010).
20. J. E. Hoffman *et al.*, *Science* **297**, 1148–1151 (2002).
21. M. P. Allan *et al.*, *Science* **336**, 563–567 (2012).
22. M. P. Allan *et al.*, *Nat. Phys.* **9**, 468–473 (2013).
23. Materials and methods are available as supplementary materials.
24. S. Mukherjee, A. Kreisel, P. J. Hirschfeld, B. M. Andersen, *Phys. Rev. Lett.* **115**, 026402 (2015).
25. A. Kreisel, S. Mukherjee, P. J. Hirschfeld, B. M. Andersen, *Phys. Rev. B* **92**, 224515 (2015).
26. Y. Suzuki *et al.*, *Phys. Rev. B* **92**, 205117 (2015).
27. M. D. Watson *et al.*, *Phys. Rev. B* **94**, 201107(R) (2016).
28. T. Terashima *et al.*, *Phys. Rev. B* **90**, 144517 (2014).
29. M. D. Watson *et al.*, *Phys. Rev. B* **91**, 155106 (2015).
30. N. Arakawa, M. Ogata, *J. Phys. Soc. Jpn.* **80**, 074704 (2011).
31. R. Yu, J.-X. Zhu, Q. Si, *Phys. Rev. B* **89**, 024509 (2014).
32. H. C. Xu *et al.*, *Phys. Rev. Lett.* **117**, 157003 (2016).
33. C.-L. Song *et al.*, *Science* **332**, 1410–1413 (2011).
34. R. Khasanov *et al.*, *Phys. Rev. B* **78**, 220510(R) (2008).
35. M. Li *et al.*, *New J. Phys.* **18**, 082001 (2016).
36. P. Bourgeois-Hope *et al.*, *Phys. Rev. Lett.* **117**, 097003 (2016).
37. S. Teknowijoyo *et al.*, *Phys. Rev. B* **94**, 064521 (2016).
38. L. Jiao *et al.*, *Sci. Rep.* **7**, 44024 (2017).
39. T. Hanaguri *et al.*, *Science* **323**, 923–926 (2009).
40. T. Hanaguri, S. Niitaka, K. Kuroki, H. Takagi, *Science* **328**, 474–476 (2010).
41. P. J. Hirschfeld, D. Altenfeld, I. Eremin, I. I. Mazin, *Phys. Rev. B* **92**, 184513 (2015).
42. D. Huang *et al.*, *Nano Lett.* **16**, 4224–4229 (2016).
43. T. Watashige *et al.*, *Phys. Rev. X* **5**, 031022 (2015).
44. Q. Wang *et al.*, *Nat. Mater.* **15**, 159–163 (2016).

ACKNOWLEDGMENTS

We are grateful to A. Chubukov, S. D. Edkins, M. H. Hamidian, J. E. Hoffman, E.-A. Kim, S. A. Kivelson, M. Lawler, D.-H. Lee, J.-H. She, and H.-H. Wen for helpful discussions and communications. J.C.S.D. and P.C.C. gratefully acknowledge support from the Moore Foundation's EPiQS (Emergent Phenomena in Quantum Physics) Initiative through grants GBMF4544 and GBMF4411, respectively. J.C.S.D. gratefully acknowledges the hospitality and support of the Tyndall National Institute, University College Cork, Cork, Ireland. P.J.H. acknowledges support from U.S. Department of Energy (DOE) grant DE-FG02-05ER46236. A.Kr. and B.M.A. acknowledge support from a Lundbeckfond Fellowship (grant A9318). Material synthesis and detailed characterization at Ames National Laboratory was supported by the U.S. DOE, Office of Basic Energy Science, Division of Materials Sciences and Engineering; Ames Laboratory is operated for the U.S. DOE by Iowa State University under contract DE-AC02-07CH11358. Experimental studies carried out by the Center for Emergent Superconductivity, an Energy Frontier Research Center, headquartered at Brookhaven National Laboratory, were funded by the U.S. DOE under grant DE-2009-BNL-PM015. The data described in the paper are archived by the Davis research group at Cornell University.

SUPPLEMENTARY MATERIALS

www.sciencemag.org/content/357/6346/75/suppl/DC1
Materials and Methods
Supplementary Text
Figs. S1 to S18
References (*45*–*63*)
Movies S1 to S3
Data S1

6 October 2016; accepted 5 June 2017
10.1126/science.aal1575

Science

Discovery of orbital-selective Cooper pairing in FeSe

P. O. Sprau, A. Kostin, A. Kreisel, A. E. Böhmer, V. Taufour, P. C. Canfield, S. Mukherjee, P. J. Hirschfeld, B. M. Andersen and J. C. Séamus Davis

Science **357** (6346), 75-80.
DOI: 10.1126/science.aal1575

A deeper look into iron selenide

In the past 10 years, iron-based superconductors have created more puzzles than they have helped resolve. Some of the most fundamental outstanding questions are how strong the interactions are and what the electron pairing mechanism is. Now two groups have made contributions toward resolving these questions in the intriguing compound iron selenide (FeSe) (see the Perspective by Lee). Gerber *et al.* used photoemission spectroscopy coupled with x-ray diffraction to find that FeSe has a very sizable electron-phonon interaction. Quasiparticle interference imaging helped Sprau *et al.* determine the shape of the superconducting gap and find that the electron pairing in FeSe is orbital-selective.

Science, this issue p. 71, p. 75; see also p. 32

Science (print ISSN 0036-8075; online ISSN 1095-9203) is published by the American Association for the Advancement of Science, 1200 New York Avenue NW, Washington, DC 20005.